Chapter 6

High Critical Current Density MgB_2

Wenxian Li and Shi-Xue Dou

Additional information is available at the end of the chapter

http://dx.doi.org/10.5772/59492

1. Introduction

The highest critical transition temperature (T_c) among all the intermetallic superconductors in that was discovered MgB_2 has changed the previous approaches to the theory of superconductivity because the T_c limit in metallic superconductors had been believed to be ~ 30 K, which is predicted by the Bardeen-Cooper-Schrieffer (BCS) theory [1]. In the BCS theory of superconductivity [2, 3], the expression for T_c is derived as $T_c = \theta e^{(-1/\lambda_{eff})}$, where θ is always equal to the MgB_2 Debye temperature, θ_D. λ_{eff} is defined as the electron and phonon coupling constant $\lambda = N(E_F) \times V$. $N(E_F)$ is the normal state electron number density the Fermi surface, and V is the average electron interaction matrix element corresponding to the attraction. A weak coupling, $\lambda << 1$, is assumed to exist between the electrons and phonons in the initial BCS theory. In this case, the value of T_c is limited to $T_c \approx 30$ K. According to the BCS theory, an element or compound with larger $N(E_F)$, V, and θ_D has high T_c value. However, θ_D of MgB_2 is comparable to those of other diborides and other light materials. Furthermore, the $N(E_F)$ is relatively low because of the absence of *d*-electrons. Thus, the unusually high T_c in MgB_2 has confused researchers with respect to the origin of its superconductivity. Considerable theoretical and experimental work has been conducted to explore the superconducting mechanism in MgB_2.

MgB_2 is the first superconductor to be proved to have two distinct superconducting gaps in its superconducting state [4]. Initially, an unconventional exotic superconducting mechanism was suggested for the material [5, 6]. Then, other researchers proposed hole superconductivity, which is similar to what occurs in high temperature superconductors (HTS), based on the fact that holes are the dominant charge carriers in the normal state [7, 8]. MgB_2 has now been accepted as a phonon-mediated BCS type superconductor. The superconductivity is attributed to selective coupling between specific electronic states and specific phonons, such as the E_{2g} mode. The unusually high T_c value arises from the strong phonon anharmonicity.

Choi *et al.* have calculated the phonon frequencies and electron-phonon interactions from frozen phonon calculations at all the symmetry points of the Brillouin zone [9]. Six non-acoustic modes at the Brillouin zone centre Γ are divided into four distinct phonon modes based on the point symmetry of the lattice. The two vibrations along the *c*-axis are singly degenerate modes of A_{2u} and B_{1g}. For the A_{2u} mode, both Mg and B move in opposite directions along *c*. For B_{1g}, the B atoms move in opposite directions, while the Mg is stationary. The other two modes along the *x* or *y* directions involving only in-plane motions are doubly degenerate. The vibration of Mg and B planes in opposite directions along the *x* or *y* directions is E_{1u} mode. Mg atoms are stationary in the E_{2g} mode, while B atoms exhibit a breathing vibration in the *x* or *y* directions. This mode is highly anharmonic. The theoretical vibration energy of the E_{2g} mode is around 75 meV [10, 11], which is in agreement with the results from Raman measurements [12, 13].

MgB_2 is easy to make into bulk, wire, tape, and thin film forms. However, the critical current density (J_c) of pristine MgB_2 drops rapidly in high magnetic field due to the weak pinning forces and low upper critical field (H_{c2}). Many techniques have been employed to improve the application potential of MgB_2, such as chemical doping, irradiation, thermo-mechanical processing, and magnetic shielding. Although the critical current density, upper critical field, and irreversibility field (H_{irr}) have been greatly increased [14], many difficulties need to be overcome for further application. The origin of the flux pinning force and relevant fabrication techniques will be discussed in this work. Lattice distortion is found to be one of the most effective sources of flux pinning centers in pure MgB_2. Then, the combined effects of connectivity and lattice disorder on the flux pinning force are investigated based on nanosize SiC doped MgB_2.

The depairing current density, J_d, can be estimated from the Ginzburg-Landau (GL) formula:

$$J_d = \Phi_0 / \left[3 / \left(\sqrt{3} \right) \pi \mu_0 \lambda^2 (T) \xi (T) \right], \tag{1}$$

where Φ_0 is the flux quantum, μ_0 the permeability of vacuum, λ the penetration depth, and ξ the coherence length [15]. However, it is not the theoretical maximum [16]. With the help of optimized pinning, about 15% of J_d can be obtained at low magnetic fields in superconductors [17, 18]. The high field values for pure MgB_2 are λ = 80 nm and ξ = 12 nm, respectively. J_d at zero K is estimated as ~1.3×10^8 A.cm^{-2}. The contribution from π-band charge carriers to the depairing current density is quite low, only about 10% [16], and the interaction energy induces the difference from the high field value. The depairing current is reduced in samples with defects because of the increased λ values [18].

The grain boundaries in MgB_2 do not show the weak link effect, and clean grain boundaries are not obstacle to supercurrents [19, 20]. On the other hand, dirty grain boundaries do potentially reduce the critical current [21]. Insulating phases on the grain boundaries, such as MgO, boron oxides [22] or boron carbide [23], normal conducting phases [24], porosity, and cracks [25], can further reduce the cross-section effective of supercurrents. The high porosity in *in-situ* prepared MgB_2 is responsible for its low density, only about half (or less) of its theoretical value [26].

http://dx.doi.org/10.5772/59492

The concept of connectivity, A_{con}, has been introduced to quantify the effective cross-section (σ_{eff}) for supercurrents [21, 27]: $A_{con} = \sigma_{eff} / \sigma_0$, where σ_0 is the geometrical cross-section. The connectivity is estimated from the phonon contribution to the normal state resistivity through $A_{con} \approx \Delta\rho_{theo}/\Delta\rho_{exp}$, with $\Delta\rho_{theo} \approx 9\ \mu\Omega$ cm. This estimate is based on the assumption that σ_{eff} is reduced equivalently in the normal and superconducting state [18]. The supercurrents are limited by the smallest effective cross-section along the conductor. A single large transverse crack can reduce strongly J_c, while only slightly increases the resistivity of a long sample. Unreacted magnesium decreases $\Delta\rho_{exp}$ [28] and the effective paths for supercurrents. The thin insulating layers located on grain boundaries can decrease the effective connectivity A_{con}, inducing high $\Delta\rho_{exp}$, although this kind of defect is transparent to supercurrents. The $\Delta\rho_{theo}$ values within the grains depend on the defects and strain in the grains. Sharma observed negative $\Delta\rho_{exp}$ in highly resistive samples [29]. Despite these objections, A_{con} is very useful for estimating the connectivity of samples if the resistivity is not too high. A clear correlation between the resistivity and the critical current was found in thin films [27]. It should be noted that this procedure is not always reliable, although it offers a possibility for understanding the influences of the connectivity on the supercurrent [18].

The *in-situ* route is a practical technique to improve the H_{c2} and J_c performance of MgB_2 using magnesium or MgH_2 as the precursor material [30-39], which reacts with boron after mixing and compacting. Low annealing temperature generates MgB_2 samples with small grains [25, 40-52] due to the poor crystallinity, and the great amount of grain boundaries result in strong pinning and high H_{c2}. Magnesium deficient samples can be fabricated by adjusting the stoichiometry of the precursor materials. This method can generate strong lattice strain in MgB_2, which decreases T_c, and increases H_{c2} [44, 53-56]. On the other hand, an excess magnesium ratio in the raw materials can compensate for the evaporation loss of Mg due to its low melting temperature and the reaction loss due to the reaction with oxygen or the sheath material. The morphology and particle size of the precursor magnesium powders are crucial for the superconductivity and superconducting performance of the final MgB_2 [57]. The grain size of the initial boron powder also has a significant influence on the MgB_2 samples. Some researchers have employed ball milling and mechanical alloying of the magnesium and boron mixture, reducing the grain size and enhancing the critical supercurrent [55, 58-65].

The reaction kinetics between magnesium and boron can be modified by chemical or compound dopants [66], which influence the grain shape and size [67, 68], the secondary phases [69], MgB_2 density [70], and the element stoichiometry [71]. Carbon doping is one of the most promising methods to improve the superconducting performance of MgB_2. The carbon sources include B_4C [72, 73], carbon [52, 66, 67, 74], carbon nanotubes [75-78], nanodiamonds [78, 79], NbC [80], SiC [41, 51, 57, 66, 72, 81-89], and organic compounds [39, 47, 90]. SiC is one of the most promising dopants because it can react with magnesium and boron to form C doped MgB_2 at quite low temperatures (600 ^oC), based on the dual reaction model [66]. Higher processing temperatures are necessary for most of the other carbon sources, leading to grain growth and worse pinning. Comparable results to those with SiC have also obtained, however, with nanoscale carbon powder [91], stearic acid [92], and carbon nanotubes [76].

The *in-situ* technique also suffers from its disadvantage of low mass density, which is originates from the annealing process, because the precursor powder has a lower density than MgB_2. High pressure synthesis increases the density [93, 94]. On the other hand, the density of *ex-situ* materials is usually close to the real density of MgB_2 [94] and can be further improved by hot isostatic pressing (HIP) [91, 95, 96]. However, the grain size of *ex-situ* produced materials is comparatively large and inhomogeneous due to the post annealing [97, 98]. Small grains (~ 100–200 nm) have also been reported [99]. A high temperature heat treatment is necessary for the *ex-situ* process to improve the connectivity [99-102]. This heat treatment leads to recrystallization and H_{c2} reduction [25]. It is concluded that disorder induced by the low temperature processing is insufficient for high superconducting performance of the *ex-situ* MgB_2. Furthermore, thermally stable defects, such as dopants, are necessary for enhancing the high field performance [18].

2. Thermal-strain-induced high J_c in high density SiC-MgB_2 bulk

The connectivity is considered to be a critical issue for improving the J_c of MgB_2 based superconductors. Furthermore, an efficient flux pinning force is crucial for high magnetic field application. Here, we employed an *in-situ* diffusion process to make high density MgB_2 bulks and investigate the efficiency of the high flux pinning force induced by lattice thermal strain [103]. Microstructural analysis and Raman scattering measurements were employed to investigate the origins of the huge flux pinning force. Doping nano-SiC particles into MgB_2 has been proven to be particularly effective in significantly enhancing J_c, H_{irr}, and H_{c2} [14, 104, 105]. In contrast to chemical doping effects, tensile stress is believed to act as a source of strong flux pinning centers when there is no reaction between SiC and MgB_2. Both the J_c and T_c are improved by thermal strain on the interface between SiC and MgB_2 during the diffusion process [106] and hybrid physical-chemical vapor deposition (HPCVD) [107]. The influences of the stress field on the flux pinning force and the electron-phonon coupling constant are discussed to clarify the superconducting performance of high density SiC-MgB_2 composite fabricated through the diffusion method.

Crystalline B with 99.999% purity was pressed into pellets or mixed with 10wt% SiC particles and then pressed into pellets. The pellets were sealed in iron tubes and padded with 99.8% Mg powder. The Mg to B atomic ratio was 1.15:2.0. The diffusion process is time dependente. The sintering condition were 1123 K for 10 h under a flow of high purity argon gas to achieve fully reacted MgB_2 bulks. Then the samples were cooled down to room temperature. X-ray diffraction (XRD) was employed to characterize the phases, and the results were refined to determine the *a*-axis and *c*-axis lattice parameters and the lattice distortion. Microstructure observations were performed with a transmission electron microscope (TEM). The magnetic J_c was derived from the height of the magnetization loop ΔM using the Bean model: $J_c = 15\Delta M/[\pi a^3 h)]$, where a and h are the radius and height of a cylindrical sample. The T_c value could be deduced from the temperature dependence curve of the magnetic susceptibility $M(T)$. To observe the temperature effects of lattice strain, Raman spectra were collected using a confocal laser Raman spectrometer (Renishaw inVia plus) under a 100× microscope. The excitation laser is Ar^+ 514.5 nm.

The density of the pure MgB_2 sample is about 1.86 g/cm^3, which is about 80% of the theoretical density. This value is much higher than those of the samples made by the *in-situ* process, which were less than 50%. The SiC-MgB_2 composite shows an even higher density of 1.91 g/cm^3 due to the SiC addition. Figure 1 shows the Rietveld refinement XRD patterns of the pure MgB_2 and the 10wt% SiC doped MgB_2 samples. In this case, SiC did not react with magnesium and boron to form C doped MgB_2 and Mg_2Si. The product is a SiC-MgB_2 composite. The Rietveld refinement analysis indicates that the unreacted SiC content was about 9.3wt%, similar to the SiC content in the precursor. This is consistent with the absence of Mg_2Si in the XRD pattern as shown in Figure 1. The result is different when the SiC-doped MgB_2 prepared by the *in-situ* technique [14, 41, 84], in which only a very small amount of SiC remaines, while Mg_2Si is always present due to the reaction of Mg with SiC. The *a*- and *c*-axis lattice parameters were 3.0850 Å and 3.5230 Å for pure MgB_2, and 3.0840 Å and 3.5282 Å for SiC doped MgB_2, respectively. The *a*-axis parameters are virtually equivalent for the two samples, whereas the *c*-axis one is slightly stretched in the SiC-MgB_2 composite. The phenomenon is different from the shortening of the *a*-axis parameter in *in-situ* processed SiC doped MgB_2, while the *c*-axis parameter remains unchanged [14, 89].

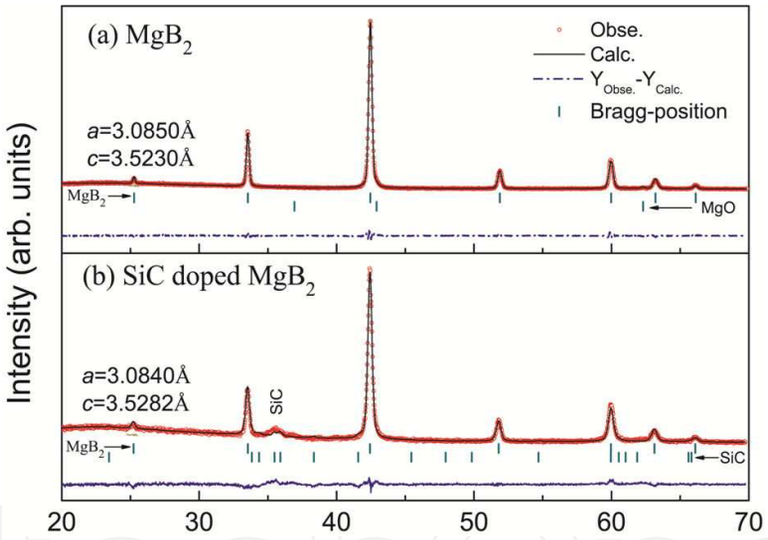

Figure 1. Rietveld refined XRD patterns of pure MgB_2 and 10wt% SiC doped MgB_2 samples made by the diffusion process at 850 °C for 10 h. The *a*-axis parameters are virtually the same for the two samples, whereas the *c*-axis paramtar is stretched in the SiC-MgB_2 composite.

To explain the abnormal *c*-axis enlargement of the SiC-MgB_2 composite, the thermal expansion coefficients, α, of MgB_2 and SiC are considered. It is reasonable to assume that both the MgB_2 and the SiC are in a stress-free state at the sintering temperature of 1123 K due to the relatively high sintering temperature over a long period of time. However, the lattice parameters are determined by the thermal strain during the cooling process. The temperature dependences of the α values for MgB_2 and SiC are especially different. Figure 2(a) plots the $\alpha(T)$ for MgB_2 and SiC along the *a*- and *c*-axes, based on the data of References [108-111]. It clearly shows the weak temperature dependence of$\alpha(T)$ for SiC in both directions, whereas the changes are great for MgB_2 and are characterized by high anisotropy. The averaged $\alpha(T)$ is also huge in MgB_2 as

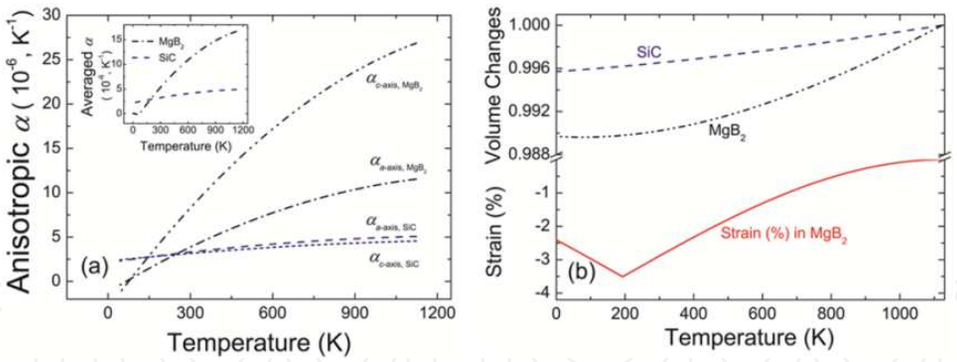

Figure 2. (a) Thermal expansion coefficients (α) along the a-axis and c-axis for MgB_2 and SiC as a function of temperature. The averaged α(T) values for MgB_2 and SiC are plotted in the inset. (b) Plots of the normalized lattice changes for MgB_2 and SiC, and the thermal strain in the matrix during cooling from 1123 K to 0 K.

shown in the inset of Figure 2(a). The α_{SiC} decreases slightly from 5×10^{-6}/K at 1123 K to 2.5×10^{-6}/K at 0 K, whereas the α_{MgB_2} drops quickly from 1.7×10^{-5}/K at 1123 K to zero at 0 K. Based on $\alpha(T)$, the normalized lattice change and lattice strain in the MgB_2 matrix of SiC-MgB_2 composite during cooling from 1123 K to 0 K can be derived, as shown in Figure 2(b). An assumption of Figure 2(b) is that the two phases are strongly connected and the volume shrinkage of MgB_2 is confined by the relatively stable SiC. The normalized lattice strain is estimated to be -0.55% in SiC-MgB_2 along the *c*-axis at room temperature. The negative value corresponds to tensile strain in the MgB_2. The large *c*-axis strain in the doped MgB_2 results in an enlargement in the *c*-axis by 0.15 % in comparison with pure MgB_2. As estimated from the Williamson-Hall model [112], the lattice strain is 0.208 and 0.306 along the *a*-axis, and 0.292 and 1.13 along the *c*-axis for pure and SiC-MgB_2, respectively. The lattice strain along the *c*-axis in the SiC-MgB_2 has increased from that of pure MgB_2 by a factor of 4, which is attributed to the high anisotropy in the thermal expansion coefficient of MgB_2.

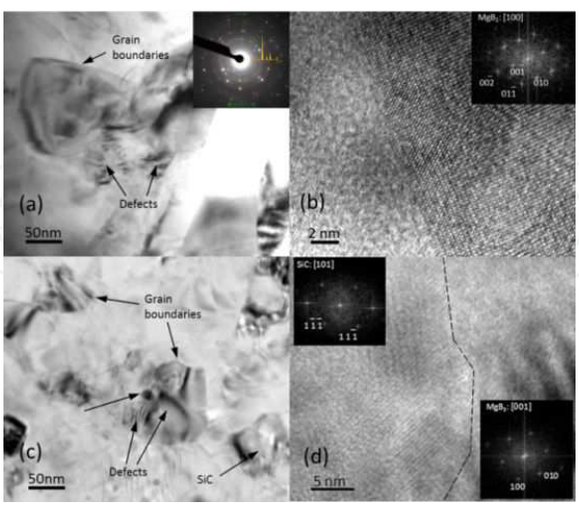

Figure 3. (a) Bright field TEM image of the pure MgB_2 with indexed SAD pattern (inset). (b) High resolution electron microscope (HREM) image of interface in pure MgB_2 with FFT pattern along the [100] axis (inset). (c) Bright field TEM image of SiC-MgB_2. (d) HREM image of interface in SiC-MgB_2 and FFT patterns of SiC and MgB_2 from each side of the interface. The dashed line shows the interface of SiC and MgB_2.

http://dx.doi.org/10.5772/59492

The unreacted SiC buried in the MgB_2 matrix is believed to be one of the most effective sources of strain, and the strongly connected interfaces of SiC and MgB_2 are the most effective flux pinning centers. The micro morphologies can be detected using TEM to explore the defects and grain boundaries both in the pure MgB_2 and in the SiC-MgB_2. Figures 3(a) shows a bright field image of pure MgB_2. A high density of defects, such as dislocations and lattice distortion, is observed in the MgB_2 phase, and the grain size is about 100 nm,as estimated from the grain boundaries. In contrast to with the highly porous structure in the MgB_2 samples [91], the samples made by the diffusion process are well connected with high density. The indexed selected area diffraction (SAD) image shows very pure polycrystalline MgB_2. A high resolution grain boundary image is shown in Figure 3(b). The interface is very clean and well connected. The indexed fast Fourier transform (FFT) pattern indicates that the right part parallels the (1 1 0) plane. The micro structure of SiC-MgB_2 is similar with that of pure MgB_2 with high density of defects. Furthermore, nanosize SiC particle are detected in the MgB_2 matrix as indicated in Figure 3(c). Figure 3(d) shows the interface of SiC and MgB_2. Based on the FFT analysis, the interface is marked with a dashed line on the image. The left side is a SiC grain paralleling the (1 0 1) plane and the right side is a MgB_2 grain paralleling the (0 0 1) plane. This kind of interface will impose tensile stress along the *c*-axis in MgB_2 because the thermal expansion coefficient for MgB_2 is highly anisotropic in the [001] direction, while that for SiC is nearly isotropic, which is responsible for the enlarged *c*-axis of MgB_2.

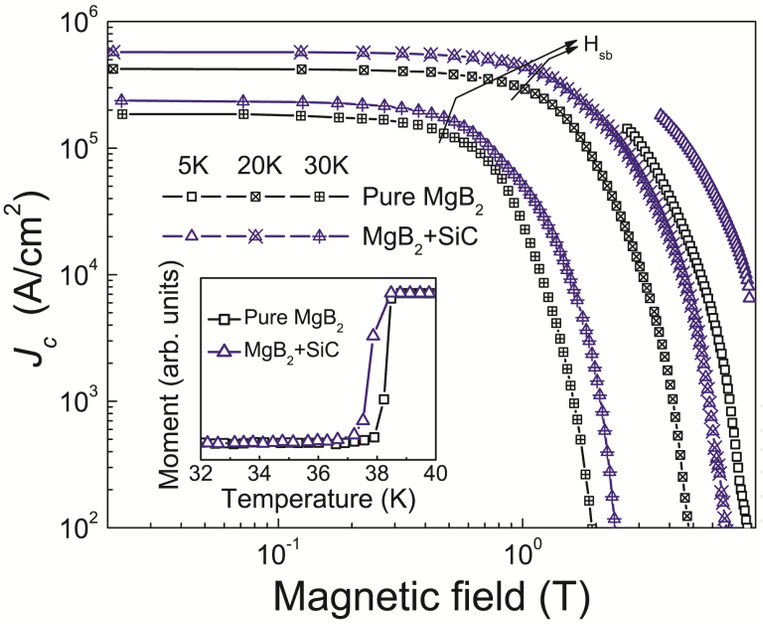

Figure 4. The magnetic J_c versus field at 5 K, 20 K, and 30 K for pure and nano-SiC doped samples. The inset shows the superconducting transitions of the two samples [103].

Based on the collective pinning model, [113], J_c is independent of the applied field in the single-vortex pinning regime (low magnetic field region: $H < H_{sb}$), where H_{sb} is the crossover field from single-vortex to small-bundle pinning. The J_c decreases exponentially in the small-bundle regime (high magnetic field: $H_{sb} < H < H_{irr}$). According to the dual model [14], the significant

effect of SiC doping on J_c comes from the high level of C substitution on the B planes, which is responsible for the reduction of the self-field J_c[104, 105]. However, the SiC-MgB_2 composite sample shows not only an improved in-field J_c, but also no degradation in self-field J_c, as indicated in Figure 4. The approximate H_{sb} values are also indicated on the J_c curves for 20 K and 30 K, although H_{sb} has not been detected at 5 K due to the relatively high supercurrents. The *in-situ* processed SiC doped MgB_2 normally shows a decrease in T_c of 1.5 to 2 K, [14, 104, 105], but this present SiC-MgB_2 composite sample features a small drop of 0.6 K, as shown in the inset of Figure 4. This phenomenon is attributed to the absence of any reaction between Mg and SiC, as well as the stretched MgB_2 lattice, as indicated by the XRD pattern [107].

To investigate whether the lattice strain is significant in SiC-MgB_2 during low temperature measurements to obtain $M(H)$ and $M(T)$ curves, Raman spectra were collected before and after the measurements. The Raman spectra for the pure MgB_2 are shown in Figure 5(a) and (b) to compare the cooling effects on the matrix. Both the spectra have been fitted with three peaks: ω_1, ω_2, and ω_3 [114-116]. Based on the previous results, ω_2 is the reflection of the E_{2g} mode at the Γ point of the Brillouin zone in the simple hexagonal MgB_2 structure (space group: *P6/mmm*), while ω_1 and ω_3 come from the lattice distortion. The effects of ω_1 are not discussed in the following analysis because of its small influence on the spectra. As indicated by the fitting parameters that are shown in Figure 5, both the peak centers and the full width at half maximum (FWHM) values show negligible differences before and after the low temperature measurements because of synchronic volume fluctuation. The weak temperature dependence of the Raman spectra for pure MgB_2 is in agreement with the results of Shi *et al* [117]. The ω_2 peak of the Raman spectrum of SiC-MgB_2 before the low temperature measurement has shifted to the low frequency of 585 cm^{-1}, as shown in Figure 6(a). The FWHM of the ω_2 peak increases from ~200 cm^{-1} to 210 cm^{-1}. Furthermore, the FWHM of the ω_3 peak increases from ~93 cm^{-1} to 125 cm^{-1}. The variations in both the Raman shift and the FWHM indicate strong lattice strain in the SiC-MgB_2 composite. Figure 6(b) shows the cooling effect on the Raman spectrum of SiC-MgB_2. The FWHM of the ω_2 peak further increases to 228 cm^{-1}, and the frequency of the ω_3 peak shifts to 770 cm^{-1}. These results suggest that the stress field is very strong during the low temperature measurements in the SiC-MgB_2 composite. Considering the stable defect structures in the sample at room temperature and the measurement temperatures, the high J_c performance is attributed to the thermal strain. Although the interface or grain boundaries themselves are effective flux pinning centers, the thermal strain provides more efficient flux pinning force, based on the comparison of the J_c values in pure the MgB_2 and the SiC-MgB_2 composite.

It should be noted that the broadened ω_2 peak in SiC-MgB_2 is a signal of strong electron-E_{2g} coupling, which is responsible for the high T_c in MgB_2. The electron-E_{2g} coupling constant is estimated from the Allen equation [118]: $\Gamma_2 = 2\pi\lambda_{E_{2g}} N(0)\omega^2_{E_{2g}}$, where Γ_2 is the ω_2 linewidth, $\lambda_{E_{2g}}$ is the strength of the electron-E_{2g} coupling, and $N(0)$ is the density of states on the Fermi surface. The experimental phonon frequency and linewidth are simply and directly related to the electron-phonon coupling constant (EPC), $\lambda_{E_{2g}}$. The total density of states (DOS) at the Fermi energy, E_F, of pure MgB_2 is taken as 0.354 states/eV/cell/spin. The σ band contribution is 0.15 and the π band is 0.204 [119]. $N(0)$ is assumed to be constant for the small changes of electrons

http://dx.doi.org/10.5772/59492

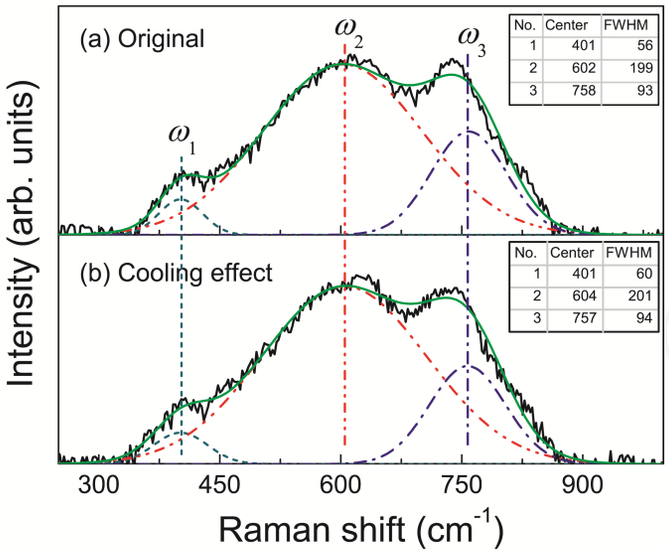

Figure 5. Fitting and experimental results for the normalized ambient Raman spectrum of MgB_2 sintered at 850 °C for 10 h (a), and the cooling effect on the Raman spectrum (b) [103].

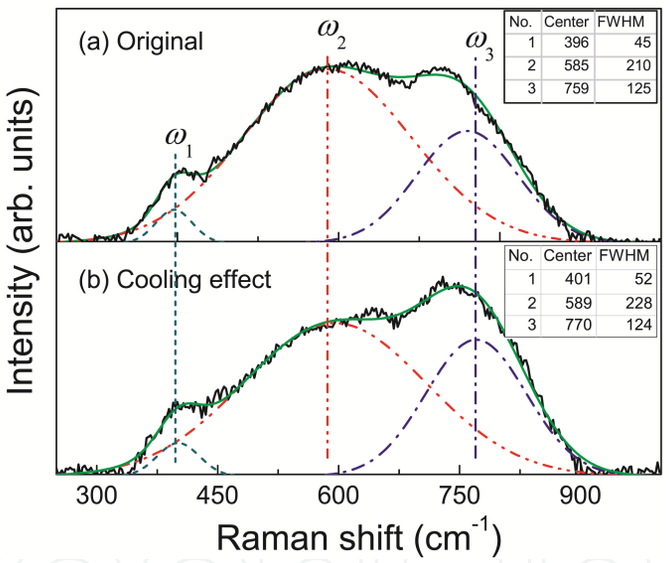

Figure 6. Fitting and experimental results for the normalized ambient Raman spectrum of SiC-MgB_2 sintered at 850 °C for 10 h (a), and the cooling effect on the Raman spectrum (b) [103].

and holes in MgB_2 and SiC-MgB_2. Taking the fitting values of the ω_2 peaks with cooling effects, the $\lambda_{E_{2g}}$ values for the pure MgB_2 and SiC-MgB_2 are 2.327 and 2.706, respectively. The $\lambda_{E_{2g}}$ of SiC-MgB_2 is just slightly higher than that of the pure MgB_2. However, the T_c of SiC-MgB_2 is slightly decreased compared to that of the pure MgB_2. The total EPC constants are degraded by the scattering effects of SiC impurities in the MgB_2 matrix, which can be estimated with the McMillan formula [120], as modified by Allen and Dynes:[121] $T_c = \frac{\langle \omega_{\log} \rangle}{1.2} \exp\left(\frac{-1.04(1+\lambda)}{\lambda - \mu^*(1+0.62\lambda)} \right)$, where $\langle \omega_{\log} \rangle = \left(390 \times \omega_{E_{2g}}^2 \times 690\right)$ is the averaged phonon frequency [122], with 390 and 690 cm^{-1}

being the phonon frequencies of the other modes in the MgB_2 system [123], μ^* is the Coulomb pseudopotential, taken as equal to 0.13 [124], and λ is the total EPC constant. Taking these values, λ is calculated as 0.888 in pure MgB_2 and 0.886 in SiC-MgB_2, respectively. Although the values are very similar, the λ of MgB_2 is a little higher because of its low impurity scattering effects. It should be noted that the λ values were overestimated using the McMillan formula for the two-gap nature of MgB_2. However, the overestimations do not change the dependence of λ on the strain effect due to the main contribution of the σ-band. The residual resistivity of SiC-MgB_2 is 16 $\mu\Omega$ cm, but it is just 12 $\mu\Omega$ cm for pure MgB_2, due to the weak impurity scattering effects.

In summary, the thermal strain originating from the interface of SiC and MgB_2 is one of the most effective sources of flux pinning centers to improve the supercurrent critical density. The weak temperature dependence of the thermal expansion coefficient of SiC stretches the MgB_2 lattice as the temperature decreases. The thermal strain supplies much more effective flux pinning force than the interfaces and grain boundaries themselves. The low temperature effects on Raman spectra include very strong lattice stretching at the application temperature of MgB_2, which has benefits from both the J_c and the T_c behaviors.

3. High connectivity MgB_2 wires fabricated by combined *in-situ*/*ex-situ* process

The self-field critical current density, $J_c(0)$, of MgB_2 is much higher than for pure or doped samples processed with *in-situ* annealing [75, 81, 125-128]. $J_c(0)$ values have been reported as high as 3.5×10^7 A/cm^2 at 4.2 K and 1.6×10^8 A/cm^2 at 2 K in highly connected thin films made by HPCVD [129, 130]. The connectivity is much lower than the theoretical value in *in-situ* MgB_2 because the technique involves a liquid-solid phase reaction process with considerable shrinkage due to the high density of MgB_2 compared to the powder mixture of Mg and B [104, 115]. Although the diffusion process could increase the J_c of bulk samples, the $J_c(0)$ and disorder of wires and tapes cannot be improved using similar methods. Several research groups have reported possible techniques to increase the connectivity of *in-situ* filamentary tapes. High pressure sintering and cold high pressure densification (CHPD) can make it possible to fabricate high density wire and tape samples [96, 131, 132]. Nevertheless, neither HIP nor CHPD are suitable for long MgB_2 wires and tapes, and the J_c values are still lower than needed for practical application. Kováč et al. reported a mixed *in-situ*/*ex-situ* process to make MgB_2 wires, and it was found that the J_c was increased when the *ex-situ* powder ratio were 23% and 50% [133]. They used commercial MgB_2 powder from Alfa Aesar in this process with a very wide grain size distribution ranging from submicrometer size up to 100 μm. In this work, high quality home-made *ex-situ* powder was used to repeat the mixed *in-situ*/*ex-situ* process to develop MgB_2/Fe wires with high connectivity and strong disorder to increase both the low and high field J_c properties [134]. The home-made powder was fabricated through low temperature annealing, and the particle size was homogeneous and as small as ~200 nm. The J_c dependence on microstruc-

ture, connectivity, and disorder in MgB_2 wires was analyzed based on the microstructure observations.

MgB_2 wires were fabricated by the powder-in-tube (PIT) process using a ball-milled mixture of Mg (99%) and amorphous B (99%). The *in-situ* wires were sintered at 750, 850, 950, and 1050 °C for 30 min in high purity Ar and marked as 750in, 850in, 950in, and 1050in, respectively. The *in-situ* MgB_2 powder was sintered at 650 °C for 30 min in high purity Ar flow and then ball-milled. Then the PIT method was employed to fabricate *in-situ/ex-situ* combined MgB_2/Fe wires using 1:3 ratio of precursor powders to form a mixture of Mg and B powders. All the green wires were annealed at 750, 850, 950, and 1050 °C for 30 min in high purity Ar and marked as 750inex, 850inex, 950inex, and 1050inex, respectively.

The phases and microstructure were characterized by XRD (D/max-2200) and field emission gun scanning electron microscopy (FEG-SEM: JSM-6700F) at room temperature. The superconducting properties were detected from 5 K to 305 K using a Physical Properties Measurement System (PPMS: Quantum Design). The critical superconducting transition temperature, T_c, is defined as the onset point on the magnetic moment *vs.* temperature curve, $M(T)$, measured in a magnetic field of 25 Oe. The magnetic J_c was derived from the Bean model. The resistivity dependence on applied magnetic field and temperature, $\rho(H, T)$, was measured using the four-probe method with H from 0 T to 13 T applied perpendicularly to the current direction, from 5 K to 305 K. H_{c2} and H_{irr} were defined as the magnetic field values at 90% and 10% on the superconducting transition on the $\rho(H, T)$ curve, respectively. The active connectivity factor, A_F, was calculated based on the $\rho(H, T)$ behavior.

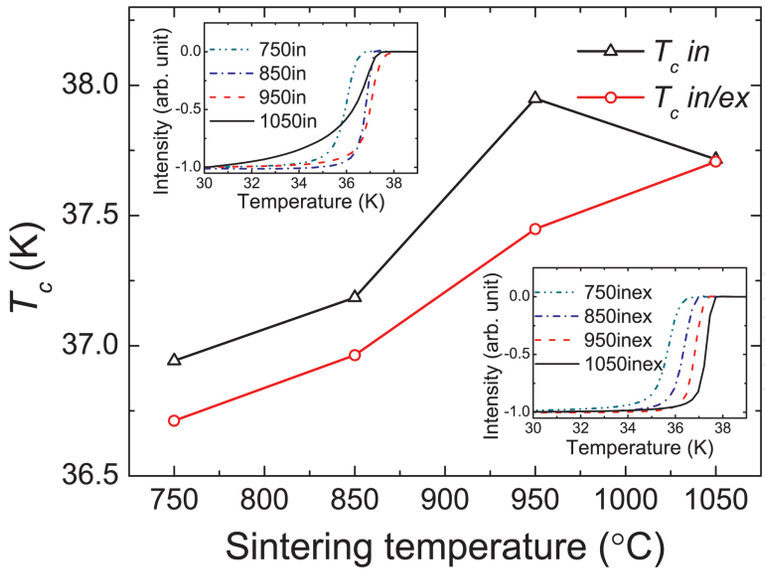

Figure 7. T_c dependence on sintering temperatures. The insets display the normalized magnetic moment dependence on measurement temperature for *in-situ* samples (upper) and for combined *in-situ/ex-situ* samples (lower) [134].

According to the indexed XRD patterns, the samples contain a small amount of MgO. The MgO contents are high in 950in, 1050in, and 1050exin compared with the other samples. The broad

transition widths from the normal state to the superconducting state of these samples confirm the high impurity contents, as shown in the insets of Figure 7. The 1050in transition width is ~7 K compared with the width of ~2 K for the other samples, which is attributed to the degraded connectivity of the magnetic flux due to the high MgO content. The *in-situ* sintered samples show higher T_c values by 0.5 – 1 K compared with the *in-situ/ex-situ* ones. The T_c of 1050in is similar to that of 1050inex because of the high amount of impurity phase. Ball milling of the raw materials induces a great amount of defects in the *in-situ/ex-situ* samples, which display lower T_c compared with the *in-situ* samples [135, 136]. The connectivity of the *in-situ/ex-situ* samples is worse than those of the *in-situ* samples judging from their big transition widths. The low amount of Mg evaporation may be responsible for the narrow transition width of 1050inex compared with that of 1050in because the stable precursor MgB_2 and low quantity of Mg in the raw materials reduce the magnesium loss during the sintering at 1050 °C.

Typical SEM images of the *in-situ* samples are shown in Figure 8. The grain size of 750in is about 300 nm, and the grains show an isolated distribution due to independent growth. 850in, 950in, and 1050in have big clusters of grains because the increasing sintering temperatures have extended the crystal growth time. Some clusters are as big as 1 μm in 1050in. The crystallinity is enhanced at higher sintering temperatures. A high sintering temperature induces raw magnesium evaporation and MgO formation, which can be observed as small white particles without contrast under SEM in 1050in.

The crystal shapes for the *in-situ/ex-situ* samples are irregular with a dispersed distribution of grain sizea, as shown in Figure 9. The grain size of 750inex is small because of the low sintering temperature. The recrystallization effect is triggered for 850inex, 950inex, and 1050inex, and big grains as large as 1 μm are observed. 1050in and 1050inex show similar microstructures because the high sintering temperature provides enough energy and a long time for the crystal growth.

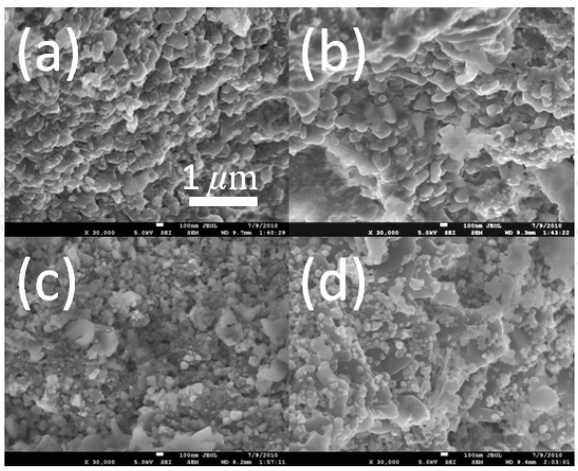

Figure 8. SEM images for the *in-situ* samples sintered at (a) 750 °C, (b) 850 °C, (c) 950 °C, and (d) 1050 °C. The crystal growth was improved gradually with increasing sintering temperature.

Figure 10 compares the J_c dependence on applied magnetic field measured at 5 K and 20 K. The J_c value of 1050in is the worst because of the high MgO content. The J_c performances of

http://dx.doi.org/10.5772/59492

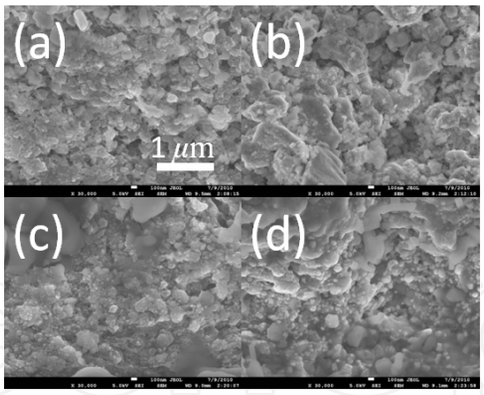

Figure 9. SEM images for the combined *in-situ/ex-situ* samples sintered at (a) 750 °C, (b) 850 °C, (c) 950 °C, and (d) 1050 °C. The grains are inhomogeneous due to the ball milled MgB_2 precursor and the recrystallization effects.

750in, 850in, 750inex, and 1050inex are quite similar over the whole field range. While the J_c deteriorated in 950in and 1050in under higher magnetic fields. 850inex and 950inex show amazingly high J_c properties. The J_c values at 5 K under 8 T magnetic field are around five times higher than those of the best *in-situ* samples. The inset of Figure 10 compares the low field performances measured at 20 K. The *in-situ* samples, except for 1050in, show competitive low field J_c. The high crystal quality of 950in is of benefit for its high self-field J_c performance. 750inex and 850inex show low self-field J_c values. While 950inex and 1050inex display improved J_c, the values are lower than the self-field J_c of 950in due to the high MgO contents.

The J_c performance depends on the flux pinning mechanism under different magnetic field intensities. The collective pinning model classifies the disorder-induced spatial fluctuations in the vortex lattice into three regimes based on the strength the magnetic field: e.g. single-vortex, small-bundle, large-bundle, and charge-density-wave type relaxation of the vortex lattice [113]. The practicable J_c of MgB_2 falls into the single-vortex pinning region and the small-bundle pinning region in the phase diagram. The connectivity determines the J_c performance in the single-vortex pinning regime because the effective charge carrier density is responsible for the self-field J_c, while H_{c2} and H_{irr} are responsible for the J_c performance in the small-bundle regime based on the disorder or defects.

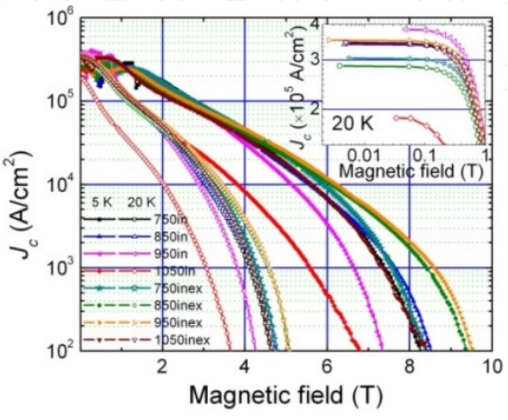

Figure 10. J_c dependence on applied magnetic field at 5 K and 20 K. The inset compares the self-field J_c behavior at 20 K [134].

A practical quantity to evaluate the connectivity is the active area fraction, A_F [21],

$$A_F = \frac{\Delta\rho_{\text{ideal}}}{\Delta\rho(300\text{K})}, \tag{2}$$

where,

$$\Delta\rho_{\text{ideal}} = \rho_{\text{ideal}}(300\text{K}) - \rho_{\text{ideal}}(40\text{K}) \approx 9\,\mu\Omega\,\text{cm}, \tag{3}$$

is the resistivity of fully connected MgB_2 without any disorder [18], and

$$\Delta\rho(300) = \rho(300K) - \rho(T_c). \tag{4}$$

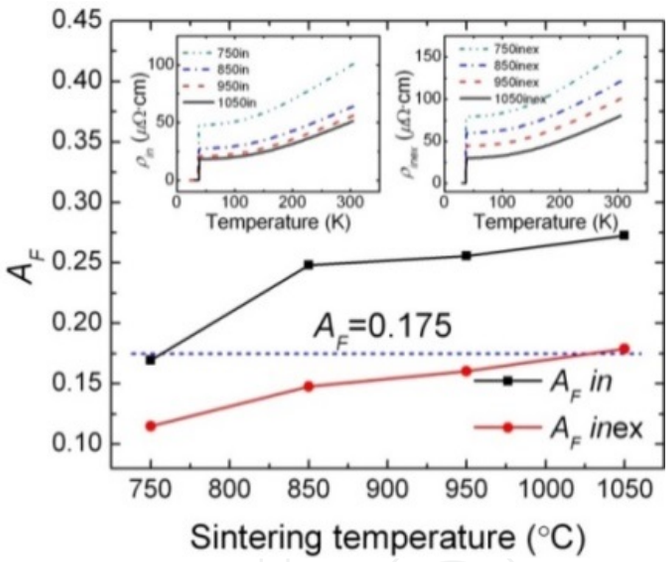

Figure 11. A_F dependence on sintering temperature. The short dashed line indicates A_F = 0.175. The upper left inset compares the resistivity of the *in-situ* samples. The upper right inset compares the resistivity of the combined *in-situ/ex-situ* samples [134].

Figure 11 compares the A_F of all the samples. All the samples show lower connectivity compared with those of ideal crystals, as indicated by the low A_F values. The A_F value of 750in is just 0.169, and high sintering temperature enhances the connectivity. It is ~ 0.26 for 850in. Higher sintering temperatures than 850 °C can improve the A_F slightly, which indicates that the connectivity is easy to improve for *in-situ* samples. Although the MgO content is high in 1050in, its high A_F value is attributed to sufficient crystallization. However, its low magnetic field J_c was degraded by MgO. The combined *in-situ/ex-situ* samples show rather low A_F values compared with the *in-situ* samples. The phenomenon is consistent with the high resistivity of the *in-situ/ex-situ* samples, as shown in the insets of Figure 11. The gradually improved

connectivity improves the A_F values for the *in-situ/ex-situ* samples due to the improved solid state reaction. The self-field J_c performances are also improved for 950inex and 1050inex.

The J_c performance in the small-bundle region depends on a strong flux pinning force. The flux pinning centers could be lattice distortion, most types of defects, and grain boundaries [110, 137]. The temperature dependences of H_{c2} and H_{irr} determine the strength of the pinning force, as shown in Figure 12. The high field J_c performance is in agreement with the H_{c2} and H_{irr} behavior. The 1050in sample shows the lowest H_{c2} and H_{irr} among all the samples. 850inex and 950inex show the highest H_{c2} and H_{irr}, which are consistent with their high J_c values in the small-bundle region. The *ex-situ* powder induces strong disorder and proper crystallization, which are responsible for the high H_{c2} and H_{irr} values.

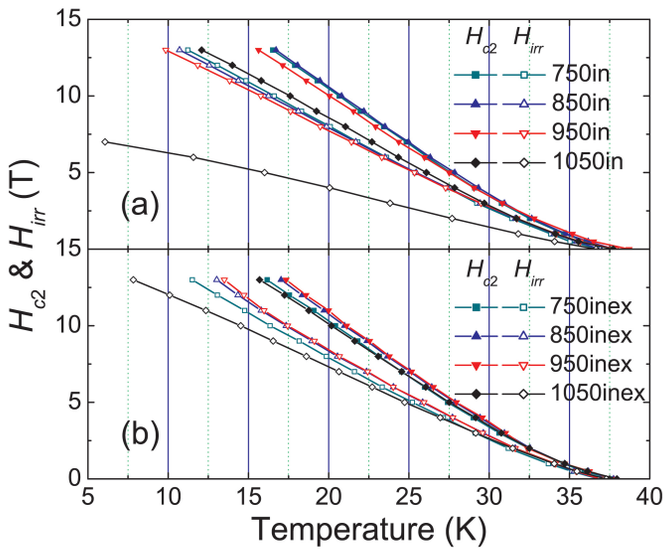

Figure 12. H_{c2} and H_{irr} of (a) the *in-situ* samples and (b) the combined *in-situ/ex-situ* samples [134].

In summary, both connectivity and disorder show strong influences on the J_c properties of MgB_2. The connectivity is responsible for the high effective charge carrier density, which determines the self-field J_c performance. The strong flux pinning force induced by defects and disorder is responsible for the promising J_c in high magnetic field. The enhanced J_c performances of 850inex and 950inex are attributed to the optimized connectivity and disorder. The J_c values obtained in this work are still far below the J_d value, ~8.7×10^8 A/cm^2 for pure MgB_2. The J_c improvement in MgB_2 should be explored based on the chemical doping effects and combined *in-situ/ex-situ* process.

4. Nano-SiC doped MgB_2 wires made by combined *In-Situ/Ex-Situ* process

The combined *in-situ/ex-situ* process has proved to be a promising technique for the fabrication of practical MgB_2 wires. The J_c of MgB_2 superconductors has been enhanced through many different kinds of dopants or additives [125], especially different carbon sources [75, 81,

126-128, 138, 139]. In this work, a mixed *in-situ/ex-situ* technique was employed to develop nano-SiC doped MgB_2 wires with high connectivity and strong flux pinning force to increase both the low and high field J_c properties [140]. The SiC particle size is another critical issue for introducing strong flux pinning forces into MgB_2. The size of SiC used in this work is smaller than the sizes used in previous research, and the J_c dependence on sintering temperature also shows a very different trend [81, 104, 141, 142].

The powder-in-tube (PIT) process was employed to make practical MgB_2 wires from a ball-milled mixture of Mg (99%), B (99%, amorphous), and SiC (< 15 nm).]The sample fabrication and characterization are similar to the techniques mentioned for the pure samples in the last section.

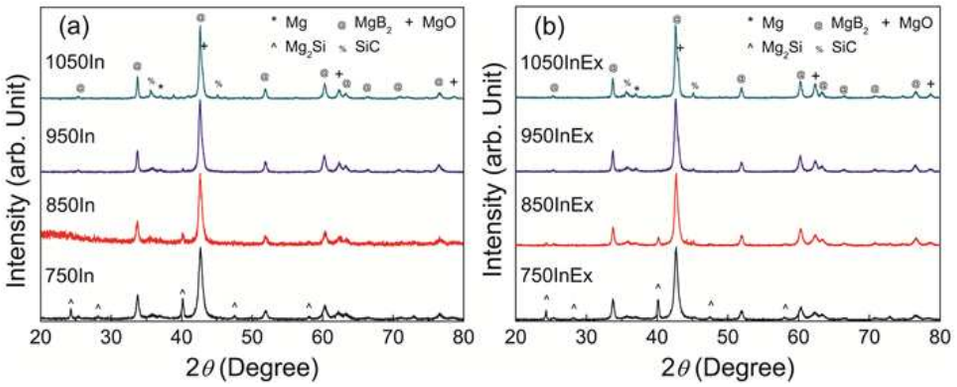

Figure 13. XRD patterns of nano-SiC doped MgB_2/Fe wires fabricated by (a) the *in-situ* technique and (b) the *in-situ/ex-situ* technique, with sintering at 750, 850, 950, and 1050 °C, respectively. All patterns were indexed with MgB_2, MgO, Mg_2Si, SiC, and Mg [140].

Figure13 shows the XRD patterns of the two batches of samples. According to the indexed XRD patterns, all samples show quite high purity of MgB_2, with only small amounts of MgO and un-reacted Mg and SiC. The un-reacted Mg can be detected because of the high content of SiC in the raw materials [104, 115, 143]. The most interesting phase change relates to the change in the Mg_2Si content with sintering temperature. 750in shows very high Mg_2Si content, which decreases with increasing sintering temperature and becomes a trace peak in 1050in. However, more than a trace of Mg_2Si can only be found in samples sintered at lower temperature using the combined *in-situ/ex-situ* method, 750inex and 850inex. The variation of Mg_2Si content is an important signal of the C and Si distributions in the MgB_2 matrix. Figure 14 shows SEM images of 850in and 850inex. The 850in sample contains large slits between MgB_2 clusters due to the volume contraction during the *in-situ* sintering of Mg and B powders. The 850inex sample shows hard-packed MgB_2 clusters because the *ex-situ* precursor is a course of nucleating centers and releases the strain of the *in-situ* MgB_2.

The critical transition temperatures (T_c) of the two batches of samples are compared in Figure 15. It is found that the T_c values of the *in-situ* sintered samples are always slightly lower than those for the samples from the other batch, except for 1050in, and the T_c dependence on sintering temperature of the two batches of samples is exactly the same, which means that the

T_c depends greatly on the sintering temperature, but not on the different techniques. However, the transition widths from the normal state to the superconducting state are quite different for the two batches of samples, as shown in the inset of Figure 15. The transition widths of the *in-situ* sintered samples are quite broad compared with those fabricated by the combined technique. The transition width is about 4 K for 750in and becomes 3 K for the 850in and 950in samples sintered at higher temperature due to the high crystallinity. It should be noted that the transition of 1050in shows a two-step behaviour, which may be attributed to the inhomogeneous carbon substitution effect or the inhomogeneous SiC distribution in the raw materials. The transition widths of all the samples made by the *in-situ/ex-situ* combined technique are 2.5 K, showing behaviour that is independent of the sintering temperature. This means that the crystallinity is increased through the *in-situ/ex-situ* combined technique because the precursor MgB_2 powder is a source of high quality nucleating centres for the newly formed MgB_2 during the solid-liquid reaction between the magnesium and the boron.

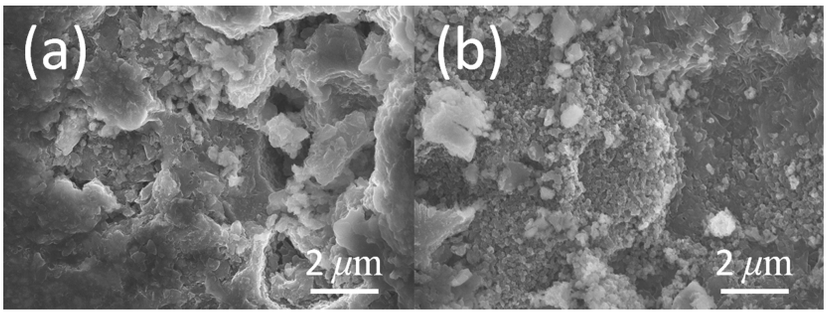

Figure 14. SEM photos of (a) 850in and (b) 850inex [140].

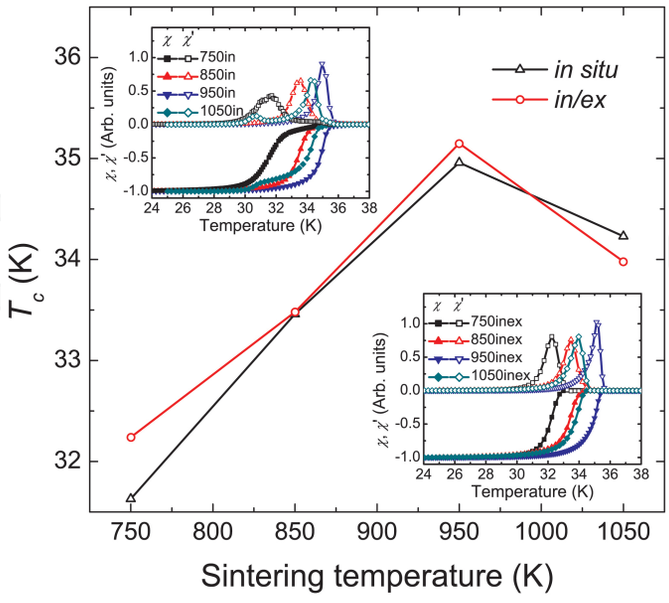

Figure 15. T_c dependence on sintering temperature. The insets show the normalized magnetic moment dependence on the measuring temperature for the *in-situ* samples (upper) and for the *in-situ/ex-situ* samples (lower) [140].

The J_c dependence on the applied field is shown in Figure 16 for typical samples, which were measured at 5 K and 20 K, respectively. It should be noted that the J_c dependence on sintering temperature in this work is totally different from previously reported results, because the solid-liquid reaction dynamics is different due to the small SiC particle size, less than 15 nm, which is much smaller than the particle sizes used before. The J_c benefits from the high sintering temperature. 750in, 850in, and 750inex display non-competitive performance over the whole field range. 1050inex has very high low field J_c values but its J_c deteriorates with increasing magnetic field. The J_c properties of 950in, 850inex, and 950inex show outstandingly high J_c performances among all the samples. It is concluded that the *in-situ/ex-situ* combined technique only requires a lower sintering temperature to achieve high quality MgB_2 wires, which is very important for industrial application in terms of energy saving and equipment simplification. The J_c values of 750inex are double those of 750in at 5 K and 20 K over the measured magnetic field range. The inset of Figure 16 displays the low field performances at 20 K to avoid the influence of the flux jumping effect. 750in and 750inex show quite low J_c values in lower magnetic field. 1050in and 850inex show competitive self-field J_c. The ball-milling process used to produce the *ex-situ* MgB_2 powder destroyes the porous structure and enhances the density of MgB_2 fabricated by the *in-situ/ex-situ* combined process. This is because of the small particle size of SiC used in this work, which induces different reaction dynamics during the *in-situ* or *in-situ/ex-situ* processing [81, 104, 141, 142], so that the present J_c dependence on sintering temperature is quite different from what has been previously reported. It is proposed that the liquid Mg reacts with SiC first to form Mg_2Si and releases free C at low sintering temperature. Then the Mg_2Si reacts with B to form MgB_2 and releases free Si at high sintering temperatures. Both C and Si have very small sizes and cannot be detected by XRD. The coherence length, ξ, of MgB_2 is anisotropic. $\xi_{ab}(0) = 3.7 – 12$ nm, and $\xi_c(0) = 1.6 - 3.6$ nm [110], which is shorter than the particle size of Mg_2Si. The Mg_2Si particles cannot be effective flux pinning centers, but are rather useless impurities in the MgB_2 matrix, which decrease the density of current carriers. However, the free C and Si can be very strong flux pinning centers because of their small sizes, which are responsible for the high J_c performance in high magnetic fields. According to the collective pinning model [113], the J_c performance in the low magnetic field region depends on the density of current carriers due to its weak field dependence, while the high magnetic field J_c performance depends on the flux pinning force due to the increased high H_{c2} and H_{irr}. The approximate H_{sb} values are also indicated on the J_c curves estimated at 20 K, as shown in the inset of Figure 16, where H_{sb} is the crossover field from single-vortex to small-bundle pinning based on the collective pinning model. However, H_{sb} has not been detected at 5 K due to the relatively high supercurrents [103].

The strength of the pinning force can be reflected by the dependence of H_{c2} and H_{irr} on the normalized temperature, as shown in Figure 17. Carbon substitution is one of the most effective methods to improve the H_{c2} and H_{irr} because of the increased scattering by C doping, and the increased scattering can also contribute to decreased T_c and merging of the two gaps [144]. It should be noted that the H_{c2} and H_{irr} for 750in, 850in, and 750inex have their highest values at low temperature, which means a strong flux pinning force. The poor J_c is of these samples attributed to the lower density of current carriers. Both 1050in and 1050inex show the lowest H_{c2} and the lowest H_{irr} among all the samples. 850in, 950in, 850inex, and 950inex show competitive H_{c2} and H_{irr} performances, which are responsible for their high J_c values under high magnetic field.

http://dx.doi.org/10.5772/59492

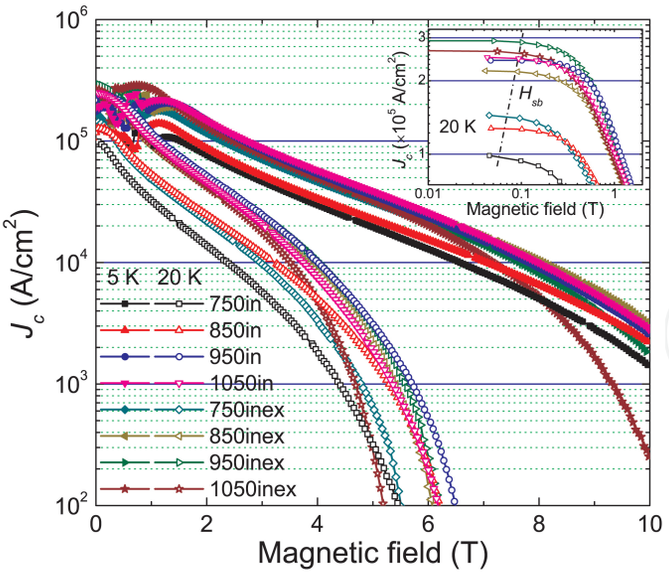

Figure 16. J_c at 5 K and 20 K. The inset indicates the J_c behavior in low magnetic field at 20 K. H_{sb}, the crossover field from single-vortex to small-bundle pinning, is indicated by the dashed-dotted line at its probable position on the J_c curves [140].

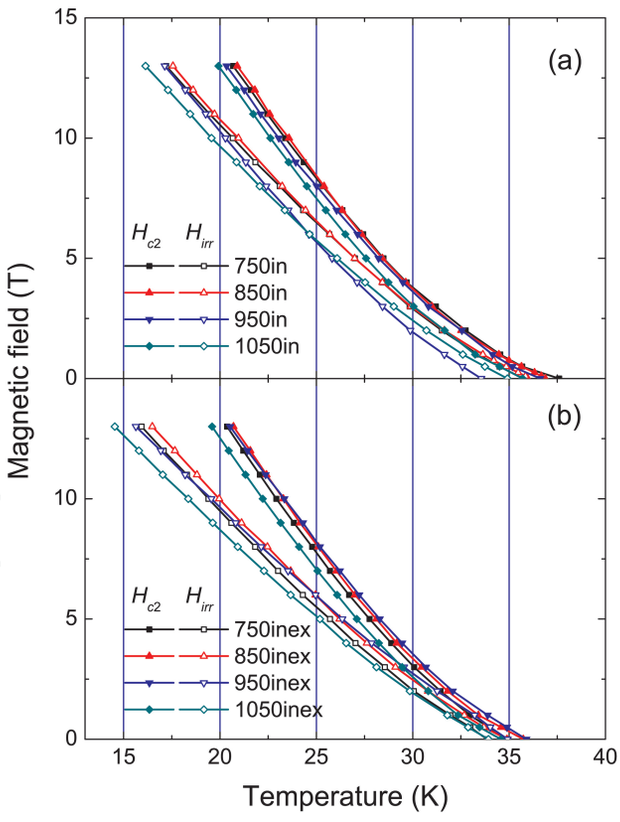

Figure 17. Comparison of H_{c2} (solid symbols) and H_{irr} (open symbols) for (a) MgB_2/Fe wires doped with nano-SiC and (b) MgB_2/Fe wires doped with nano-SiC, with sintering at 750, 850, 950, and 1050 °C, respectively [140].

In conclusion, high sintering temperature can improve the critical current density of small-particle-size SiC doped MgB_2. The two-step reactions between Mg, SiC, and B release free C and Si to form strong flux pinning centers. The current carrier density and flux pinning force are important factors in the improvement of the J_c performance of nano-SiC doped MgB_2. The current carrier density determines the J_c behavior in the single-vortex regime, where J_c is independent of applied magnetic field. The flux pinning force determines the J_c performance in the small-bundle pinning regime, where the doping induced defects are believed to act as flux pinning centers. Nano-SiC doped MgB_2/Fe wires fabricated by the combined process are worth ongoing research to develop optimized processing parameters for practical purposes.

5. Conclusions

The diffusion method can greatly improve the critical current density compared with the normal technique, which indicates that the critical current density greatly depends on the connectivity of MgB_2 grains. The combined process improves the connectivity of MgB_2 grains and the compactness of the superconducting core in wires, which induces high critical current density in zero field. The flux pinning force can also be improved by dopants for magnetic field application. Further research could focus on parameter optimization of the combined process to fabricate high quality MgB_2 wires.

Acknowledgements

The authors thank Dr. T. Silver for her useful discussions. This work is supported by the Program for Professor of Special Appointment (Eastern Scholar) at Shanghai Institutions of Higher Learning, the Australian Research Council (project ID: DP0770205), and Hyper Tech Research Inc.

Author details

Wenxian Li[1,2,3*] and Shi-Xue Dou[2]

*Address all correspondence to: shuliwx@shu.edu.cn

1 School of Materials Science & Engineering, Shanghai University, Shanghai, China

2 Institute for Superconducting & Electronic Materials, University of Wollongong, Wollongong, Australia

3 School of Computing, Engineering & Mathematics, University of Western Sydney, Sydney, Australia

http://dx.doi.org/10.5772/59492

References

[1] Nagamatsu J, Nakagawa N, Muranaka T, Zenitani Y, and Akimitsu J, Superconductivity at 39 K in magnesium diboride, Nature 2001; 410(6824) 63-64.

[2] Ginzburg VL, Nobel Lecture: On superconductivity and superfluidity (what I have and have not managed to do) as well as on the "physical minimum" at the beginning of the XXI century, Rev. Mod. Phys. 2004; 76(3) 981-998.

[3] Bardeen J, Cooper LN, and Schrieffer JR, Theory of Superconductivity, Phys. Rev. 1957; 108(5) 1175-1204.

[4] Canfield PC and Crabtree G, Magnesium diboride: Better late than never, Phys. Today 2003; 56(3) 34-40.

[5] Ivanov VA, van den Broek M, and Peeters FM, Strongly interacting sigma-electrons and MgB_2 superconductivity, Solid State Commun. 2001; 120(2-3) 53-57.

[6] Baskaran G, Resonating-valence-bond contribution to superconductivity in MgB_2, Phys. Rev. B 2002; 65(21) 212505.

[7] Hirsch JE, Hole superconductivity in MgB_2: a high T_c cuprate without Cu, Phys. Lett. A 2001; 282(6) 392-398.

[8] Hirsch JE and Marsiglio F, Electron-phonon or hole superconductivity in (MgB_2), Phys. Rev. B 2001; 64(14) 144532.

[9] Choi HJ, Cohen ML, and Louie SG, Anisotropic Eliashberg theory of MgB_2: T_c, isotope effects, superconducting energy gaps, quasiparticles, and specific heat, Physica C 2003; 385(1-2) 66-74.

[10] Yildirim T, Gulseren O, Lynn JW, Brown CM, Udovic TJ, Huang Q, Rogado N, Regan KA, Hayward MA, Slusky JS, He T, Haas MK, Khalifah P, Inumaru K, and Cava RJ, Giant anharmonicity and nonlinear electron-phonon coupling in MgB_2: A combined first-principles calculation and neutron scattering study, Phys. Rev. Lett. 2001; 87(3) 037001.

[11] Liu AY, Mazin II, and Kortus J, Beyond Eliashberg superconductivity in MgB_2: Anharmonicity, two-phonon scattering, and multiple gaps, Phys. Rev. Lett. 2001; 87(8) 087005.

[12] Hlinka J, Gregora I, Pokorny J, Plecenik A, Kus P, Satrapinsky L, and Benacka S, Phonons in MgB_2 by polarized Raman scattering on single crystals, Phys. Rev. B 2001; 64(14) 140503.

[13] Goncharov AF, Struzhkin VV, Gregoryanz E, Hu JZ, Hemley RJ, Mao HK, Lapertot G, Bud'ko SL, and Canfield PC, Raman spectrum and lattice parameters of MgB_2 as a function of pressure, Phys. Rev. B 2001; 64(10) 100509.

[14] Dou SX, Shcherbakova O, Yeoh WK, Kim JH, Soltanian S, Wang XL, Senatore C, Flukiger R, Dhalle M, Husnjak O, and Babic E, Mechanism of enhancement in electromagnetic properties of MgB_2 by nano SiC doping, Phys. Rev. Lett. 2007; 98(9) 097002.

[15] Tinkham M, Introduction to Superconductivity, 2nd ed., New York: McGraw-Hill,, 1996; 123.

[16] Nicol EJ and Carbotte JP, Theory of the critical current in two-band superconductors with application to MgB_2, Phys. Rev. B 2005; 72(1) 014520.

[17] Arcos DH and Kunchur MN, Suppressed flux motion in magnesium diboride films, Phys. Rev. B 2005; 71(18) 184516.

[18] Eisterer M, Magnetic properties and critical currents of MgB_2, Supercond. Sci. Technol. 2007; 20(12) R47-R73.

[19] Finnemore DK, Ostenson JE, Bud'ko SL, Lapertot G, and Canfield PC, Thermodynamic and transport properties of superconducting $Mg^{10}B_2$, Phys. Rev. Lett. 2001; 86(11) 2420-2422.

[20] Kawano K, Abell JS, Kambara M, Babu NH, and Cardwell DA, Evidence for high intergranular current flow in a single-phase polycrystalline MgB_2 superconductor, Appl. Phys. Lett. 2001; 79(14) 2216-2218.

[21] Rowell JM, The widely variable resistivity of MgB_2 samples, Supercond. Sci. Technol. 2003; 16(6) R17-R27.

[22] Klie RF, Idrobo JC, Browning ND, Regan KA, Rogado NS, and Cava RJ, Direct observation of nanometer-scale Mg- and B-oxide phases at grain boundaries in MgB_2, Appl. Phys. Lett. 2001; 79(12) 1837-1839.

[23] Pogrebnyakov AV, Xi XX, Redwing JM, Vaithyanathan V, Schlom DG, Soukiassian A, Mi SB, Jia CL, Giencke JE, Eom CB, Chen J, Hu YF, Cui Y, and Li Q, Properties of MgB_2 thin films with carbon doping, Appl. Phys. Lett. 2004; 85(11) 2017-2019.

[24] Hassler W, Birajdar B, Gruner W, Herrmann M, Perner O, Rodig C, Schubert M, Holzapfel B, Eibl O, and Schultz L, MgB_2 bulk and tapes prepared by mechanical alloying: influence of the boron precursor powder, Supercond. Sci. Technol. 2006; 19(6) 512-520.

[25] Fischer C, Hassler W, Rodig C, Perner O, Behr G, Schubert M, Nenkov K, Eckert J, Holzapfel B, and Schultz L, Critical current densities of superconducting MgB_2 tapes prepared on the base of mechanically alloyed precursors, Physica C 2004; 406(1-2) 121-130.

[26] Yeoh WK, Kim JH, Horvat J, Dou SX, and Munroe P, Improving flux pinning of MgB_2 by carbon nanotube doping and ultrasonication, Supercond. Sci. Technol. 2006; 19(2) L5-L8.

[27] Rowell JM, Xu SY, Zeng H, Pogrebnyakov AV, Li Q, Xi XX, Redwing JM, Tian W, and Pan XQ, Critical current density and resistivity of MgB_2 films, Appl. Phys. Lett. 2003; 83(1) 102-104.

[28] Kim KH, Betts JB, Jaime M, Lacerda AH, Boebinger GS, Jung CU, Kim HJ, Park MS, and Lee SI, Mg as a main source for the diverse magnetotransport properties of MgB_2, Phys. Rev. B 2002; 66(2) 020506.

[29] Sharma PA, Hur N, Horibe Y, Chen CH, Kim BG, Guha S, Cieplak MZ, and Cheong SW, Percolative superconductivity in $Mg_{1-x}B_2$, Phys. Rev. Lett. 2002; 89(16) 167003.

[30] Kumakura H, Kitaguchi H, Matsumoto A, and Yamada H, Upper critical field, irreversibility field, and critical current density of powder-in-tube-processed MgB_2/Fe tapes, Supercond. Sci. Technol. 2005; 18(8) 1042-1046.

[31] Nakane T, Jiang CH, Mochiku T, Fujii H, Kuroda T, and Kumakura H, Effect of SiC nanoparticle addition on the critical current density of MgB_2 tapes fabricated from MgH_2, B and MgB_2 powder mixtures, Supercond. Sci. Technol. 2005; 18(10) 1337-1341.

[32] Hata S, Yoshidome T, Sosiati H, Tomokiyo Y, Kuwano N, Matsumoto A, Kitaguchi H, and Kumakura H, Microstructures of MgB_2/Fe tapes fabricated by an powder-in-tube method using MgH_2 as a precursor powder, Supercond. Sci. Technol. 2006; 19(2) 161-168.

[33] Jiang CH, Hatakeyama H, and Kumakura H, Preparation of MgB_2/Fe tapes with improved J_c property using MgH_2 powder and a short pre-annealing and intermediate rolling process, Supercond. Sci. Technol. 2005; 18(5) L17-L22.

[34] Fujii H, Togano K, and Kumakura H, Enhancement of critical current densities of powder-in-tube processed MgB_2 tapes by using MgH_2 as a precursor powder, Supercond. Sci. Technol. 2002; 15(11) 1571-1576.

[35] Jiang CH, Nakane T, Hatakeyama H, and Kumakura H, Enhanced J_c property in nano-SiC doped thin MgB_2/Fe wires by a modified PIT process, Physica C 2005; 422(3-4) 127-131.

[36] Jiang CH, Hatakeyama H, and Kumakura H, Effect of nanometer MgO addition on the PIT processed MgB_2/Fe tapes, Physica C 2005; 423(1-2) 45-50.

[37] Matsumoto A, Kumakura H, Kitaguchi H, and Hatakeyama H, Effect of SiO_2 and SiC doping on the powder-in-tube processed MgB_2 tapes, Supercond. Sci. Technol. 2003; 16(8) 926-930.

[38] Pachla W, Morawski A, Kovac P, Husek I, Mazur A, Lada T, Diduszko R, Melisek T, Strbik V, and Kulczyk M, Properties of hydrostatically extruded *in situ* MgB_2 wires doped with SiC, Supercond. Sci. Technol. 2006; 19(1) 1-8.

[39] Yamada H, Hirakawa M, Kumakura H, and Kitaguchi H, Effect of aromatic hydrocarbon addition on *in situ* powder-in-tube processed MgB_2 tapes, Supercond. Sci. Technol. 2006; 19(2) 175-177.

[40] Goldacker W, Schlachter SI, Obst B, Liu B, Reiner J, and Zimmer S, Development and performance of thin steel reinforced MgB_2 wires and low-temperature processing for further improvements, Supercond. Sci. Technol. 2004; 17(5) S363-S368.

[41] Matsumoto A, Kumakura H, Kitaguchi H, Senkowicz BJ, Jewell MC, Hellstrom EE, Zhu Y, Voyles PM, and Larbalestier DC, Evaluation of connectivity, flux pinning, and upper critical field contributions to the critical current density of bulk pure and SiC-alloyed MgB_2, Appl. Phys. Lett. 2006; 89(13) 132508.

[42] Yamamoto A, Shimoyama J, Ueda S, Iwayama I, Horii S, and Kishio K, Effects of B_4C doping on critical current properties of MgB_2 superconductor, Supercond. Sci. Technol. 2005; 18(10) 1323-1328.

[43] Perner O, Habler W, Eckert R, Fischer C, Mickel C, Fuchs G, Holzapfel B, and Schultz L, Effects of oxide particle addition on superconductivity in nanocrystalline MgB_2 bulk samples, Physica C 2005; 432(1-2) 15-24.

[44] Jiang CH, Nakane T, and Kumakura H, Superior high-field current density in slightly Mg-deficient MgB_2 tapes, Appl. Phys. Lett. 2005; 87(25) 252505.

[45] Wu YF, Lu YF, Yan G, Li JS, Feng Y, Tang HP, Chen SK, Xu HL, Li CS, and Zhang PX, Improved superconducting properties in bulk MgB_2 prepared by high-energy milling of Mg and B powders, Supercond. Sci. Technol. 2006; 19(11) 1215-1218.

[46] Kim JH, Yeoh WK, Qin MJ, Xu X, and Dou SX, The doping effect of multiwall carbon nanotube on MgB_2/Fe superconductor wire, J. Appl. Phys. 2006; 100(1) 013908.

[47] Kim JH, Zhou S, Hossain MSA, Pan AV, and Dou SX, Carbohydrate doping to enhance electromagnetic properties of MgB_2 superconductors, Appl. Phys. Lett. 2006; 89(14) 142505.

[48] Chen SK, Lockman Z, Wei M, Glowacki BA, and MacManus-Driscoll JL, Improved current densities in MgB_2 by liquid-assisted sintering, Appl. Phys. Lett. 2005; 86(24) 242501.

[49] Ueda S, Shimoyama J, Iwayama I, Yamamoto A, Katsura Y, Horii S, and Kishio K, High critical current properties of MgB_2 bulks prepared by a diffusion method, Appl. Phys. Lett. 2005; 86(22) 222502.

[50] Zhang XP, Gao ZS, Wang DL, Yu ZG, Ma YW, Awaji S, and Watanabe K, Improved critical current densities in MgB_2 tapes with ZrB_2 doping, Appl. Phys. Lett. 2006; 89(13) 132510.

[51] Shcherbakova O, Dou SX, Soltanian S, Wexler D, Bhatia M, Sumption M, and Collings EW, The effect of doping level and sintering temperature on $J_c(H)$ performance in nano-SiC doped and pure MgB_2 wires, J. Appl. Phys. 2006; 99(8) 08M510.

[52] Ma YW, Zhang XP, Nishijima G, Watanabe K, Awaji S, and Bai XD, Significantly enhanced critical current densities in MgB_2 tapes made by a scaleable nanocarbon addition route, Appl. Phys. Lett. 2006; 88(7) 072502.

[53] Ribeiro RA, Bud'ko SL, Petrovic C, and Canfield PC, Effects of boron purity, Mg stoichiometry and carbon substitution on properties of polycrystalline MgB_2, Physica C 2003; 385(1-2) 16-23.

[54] Liao XZ, Serquis A, Zhu YT, Peterson DE, Mueller FM, and Xu HF, Strain effect on the critical superconducting temperature of MgB_2, Supercond. Sci. Technol. 2004; 17(8) 1026-1030.

[55] Perner O, Eckert J, Hassler W, Fischer C, Acker J, Gemming T, Fuchs G, Holzapfel B, and Schultz L, Stoichiometry dependence of superconductivity and microstructure in mechanically alloyed MgB_2, J. Appl. Phys. 2005; 97(5) 056105.

[56] Serquis A, Zhu YT, Peterson EJ, Coulter JY, Peterson DE, and Mueller FM, Effect of lattice strain and defects on the superconductivity of MgB_2, Appl. Phys. Lett. 2001; 79(26) 4399-4401.

[57] Yamada H, Hirakawa M, Kumakura H, Matsumoto A, and Kitaguchi H, Critical current densities of powder-in-tube MgB_2 tapes fabricated with nanometer-size Mg powder, Appl. Phys. Lett. 2004; 84(10) 1728-1730.

[58] Fang H, Padmanabhan S, Zhou YX, and Salama K, High critical current density in iron-clad MgB_2 tapes, Appl. Phys. Lett. 2003; 82(23) 4113-4115.

[59] Fischer C, Rodig C, Hassler W, Perner O, Eckert J, Nenkov K, Fuchs G, Wendrock H, Holzapfel B, and Schultz L, Preparation of MgB_2 tapes using a nanocrystalline partially reacted precursor, Appl. Phys. Lett. 2003; 83(9) 1803-1805.

[60] Strickland NM, Buckley RG, and Otto A, High critical current densities in Cu-sheathed MgB_2 formed from a mechanically-alloyed precursor, Appl. Phys. Lett. 2003; 83(2) 326-328.

[61] Flukiger R, Suo HL, Musolino N, Beneduce C, Toulemonde P, and Lezza P, Superconducting properties of MgB_2 tapes and wires, Physica C 2003; 385(1-2) 286-305.

[62] Goldacker W, Schlachter SI, Liu B, Obst B, and Klimenko E, Considerations on critical currents and stability of MgB_2 wires made by different preparation routes, Physica C 2004; 401(1-4) 80-86.

[63] Flukiger R, Lezza P, Beneduce C, Musolino N, and Suo HL, Improved transport critical current and irreversibility fields in mono- and multifilamentary Fe/MgB_2 tapes and wires using fine powders, Supercond. Sci. Technol. 2003; 16(2) 264-270.

[64] Grovenor CRM, Goodsir L, Salter CJ, Kovac P, and Husek I, Interfacial reactions and oxygen distribution in MgB_2 wires in Fe, stainless steel and Nb sheaths, Supercond. Sci. Technol. 2004; 17(3) 479-484.

[65] Senkowicz BJ, Giencke JE, Patnaik S, Eom CB, Hellstrom EE, and Larbalestier DC, Improved upper critical field in bulk-form magnesium diboride by mechanical alloying with carbon, Appl. Phys. Lett. 2005; 86(20) 202502.

[66] Dou SX, Shcherbakova O, Yoeh WK, Kim JH, Soltanian S, Wang XL, Senatore C, Flukiger R, Dhalle M, Husnjak O, and Babic E, Mechanism of enhancement in electromagnetic properties of MgB_2 by nano SiC doping, Phys. Rev. Lett. 2007; 98(9) 097002.

[67] Zhao Y, Feng Y, Shen TM, Li G, Yang Y, and Cheng CH, Cooperative doping effects of Ti and C on critical current density and irreversibility field of MgB_2, J. Appl. Phys. 2006; 100(12) 123902.

[68] Xu X, Kim JH, Yeoh WK, Zhang Y, and Dou SX, Improved J_c of MgB_2 superconductor by ball milling using different media, Supercond. Sci. Technol. 2006; 19(11) L47-L50.

[69] Haigh S, Kovac P, Prikhna TA, Savchuk YM, Kilburn MR, Salter C, Hutchison J, and Grovenor C, Chemical interactions in Ti doped MgB_2 superconducting bulk samples and wires, Supercond. Sci. Technol. 2005; 18(9) 1190-1196.

[70] Ma YW, Kumakura H, Matsumoto A, Hatakeyama H, and Togano K, Improvement of critical current density in Fe-sheathed MgB_2 tapes by $ZrSi_2$, ZrB_2 and WSi_2 doping, Supercond. Sci. Technol. 2003; 16(8) 852-856.

[71] Kumar D, Pennycook SJ, Narayan J, Wang H, and Tiwari A, Role of silver addition in the synthesis of high critical current density MgB_2 bulk superconductors, Supercond. Sci. Technol. 2003; 16(4) 455-458.

[72] Yamamoto A, Shimoyama J, Ueda S, Katsura Y, Iwayama I, Horii S, and Kishio K, Universal relationship between crystallinity and irreversibility field of MgB_2, Appl. Phys. Lett. 2005; 86(21) 212502.

[73] Lezza P, Senatore C, and Flukiger R, Improved critical current densities in B_4C doped MgB_2 based wires, Supercond. Sci. Technol. 2006; 19(10) 1030-1033.

[74] Yeoh WK, Kim JH, Horvat J, Xu X, Qin MJ, Dou SX, Jiang CH, Nakane T, Kumakura H, and Munroe P, Control of nano carbon substitution for enhancing the critical current density in MgB_2, Supercond. Sci. Technol. 2006; 19(6) 596-599.

[75] Dou SX, Yeoh WK, Horvat J, and Ionescu M, Effect of carbon nanotube doping on critical current density of MgB_2 superconductor, Appl. Phys. Lett. 2003; 83(24) 4996-4998.

[76] Kim JH, Yeoh WK, Qin MJ, Xu X, Dou SX, Munroe P, Kumakura H, Nakane T, and Jiang CH, Enhancement of in-field J_c in MgB_2/Fe wire using single- and multiwalled carbon nanotubes, Appl. Phys. Lett. 2006; 89(12) 122510.

[77] Kovac P, Husek I, Skakalova V, Meyer J, Dobrocka E, Hirscher M, and Roth S, Transport current improvements of *in situ* MgB_2 tapes by the addition of carbon nanotubes, silicon carbide or graphite, Supercond. Sci. Technol. 2007; 20(1) 105-111.

[78] Cheng CH, Yang Y, Munroe P, and Zhao Y, Comparison between nano-diamond and carbon nanotube doping effects on critical current density and flux pinning in MgB_2, Supercond. Sci. Technol. 2007; 20(3) 296-301.

[79] Cheng CH, Zhang H, Zhao Y, Feng Y, Rui XF, Munroe P, Zeng HM, Koshizuka N, and Murakami M, Doping effect of nano-diamond on superconductivity and flux pinning in MgB_2, Supercond. Sci. Technol. 2003; 16(10) 1182-1186.

[80] Gao ZS, Zhang XP, Wang DL, Liu X, Li XH, Ma YW, and Mossang E, Effects of NbC addition on the critical current density of MgB_2 tapes, Supercond. Sci. Technol. 2007; 20(1) 57-61.

[81] Dou SX, Soltanian S, Horvat J, Wang XL, Zhou SH, Ionescu M, Liu HK, Munroe P, and Tomsic M, Enhancement of the critical current density and flux pinning of MgB_2 superconductor by nanoparticle SiC doping, Appl. Phys. Lett. 2002; 81(18) 3419-3421.

[82] Soltanian S, Wang XL, Horvat J, Dou SX, Sumption MD, Bhatia M, Collings EW, Munroe P, and Tomsic M, High transport critical current density and large H_{c2} and H_{irr} in nanoscale SiC doped MgB_2 wires sintered at low temperature, Supercond. Sci. Technol. 2005; 18(5) 658-666.

[83] Chen SK, Tan KS, Glowacki BA, Yeoh WK, Soltanian S, Horvat J, and Dou SX, Effect of heating rates on superconducting properties of pure MgB_2, carbon nanotube- and nano-SiC-doped MgB_2/Fe wires, Appl. Phys. Lett. 2005; 87(18) 182504.

[84] Dou SX, Braccini V, Soltanian S, Klie R, Zhu Y, Li S, Wang XL, and Larbalestier D, Nanoscale-SiC doping for enhancing J_c and H_{c2} in superconducting MgB_2, J. Appl. Phys. 2004; 96(12) 7549-7555.

[85] Ma YW, Zhang XP, Xu AX, Li XH, Xiao LY, Nishijima G, Awaji S, Watanabe K, Jiao YL, Xiao L, Bai XD, Wu KH, and Wen HH, The effect of $ZrSi_2$ and SiC doping on the microstructure and J_c-B properties of PIT processed MgB_2 tapes, Supercond. Sci. Technol. 2006; 19(1) 133-137.

[86] Sumption MD, Bhatia M, Rindfleisch M, Tomsic M, and Collings EW, Transport and magnetic J_c of MgB_2 strands and small helical coils, Appl. Phys. Lett. 2005; 86(10) 102501.

[87] Kumakura H, Kitaguchi H, Matsumoto A, and Hatakeyama H, Upper critical fields of powder-in-tube-processed MgB_2/Fe tape conductors, Appl. Phys. Lett. 2004; 84(18) 3669-3671.

[88] Li S, White T, Laursen K, Tan TT, Sun CQ, Dong ZL, Li Y, Zho SH, Horvat J, and Dou SX, Intense vortex pinning enhanced by semicrystalline defect traps in self-aligned nanostructured MgB_2, Appl. Phys. Lett. 2003; 83(2) 314-316.

[89] Sumption MD, Bhatia M, Rindfleisch M, Tomsic M, Soltanian S, Dou SX, and Collings EW, Large upper critical field and irreversibility field in MgB_2 wires with SiC additions, Appl. Phys. Lett. 2005; 86(9) 092507.

[90] Hossain MSA, Kim JH, Wang XL, Xu X, Peleckis G, and Dou SX, Enhancement of flux pinning in a MgB_2 superconductor doped with tartaric acid, Supercond. Sci. Technol. 2007; 20(1) 112-116.

[91] Liao XZ, Serquis A, Zhu YT, Civale L, Hammon DL, Peterson DE, Mueller FM, Nesterenko VF, and Gu Y, Defect structures in MgB_2 wires introduced by hot isostatic pressing, Supercond. Sci. Technol. 2003; 16(7) 799-803.

[92] Gao ZS, Ma YW, Zhang XP, Wang DL, Yu ZG, Watanabe K, Yang HA, and Wen HH, Strongly enhanced critical current density in MgB_2/Fe tapes by stearic acid and stearate doping, Supercond. Sci. Technol. 2007; 20(5) 485-489.

[93] Wen HH, Li SL, Zhao ZW, Jin H, Ni YM, Ren ZA, Che GC, and Zhao ZX, Magnetic relaxation and critical current density of the new superconductor MgB_2, Supercond. Sci. Technol. 2002; 15(3) 315-319.

[94] Prikhna TA, Gawalek W, Savchuk YM, Moshchil VE, Sergienko NV, Habisreuther T, Wendt M, Hergt R, Schmidt C, Dellith J, Melnikov VS, Assmann A, Litzkendorf D, and Nagorny PA, High-pressure synthesis of MgB_2 with addition of Ti, Physica C 2004; 402(3) 223-233.

[95] Serquis A, Liao XZ, Zhu YT, Coulter JY, Huang JY, Willis JO, Peterson DE, Mueller FM, Moreno NO, Thompson JD, Nesterenko VF, and Indrakanti SS, Influence of microstructures and crystalline defects on the superconductivity of MgB_2, J. Appl. Phys. 2002; 92(1) 351-356.

[96] Serquis A, Civale L, Hammon DL, Liao XZ, Coulter JY, Zhu YT, Jaime M, Peterson DE, Mueller FM, Nesterenko VF, and Gu Y, Hot isostatic pressing of powder in tube MgB_2 wires, Appl. Phys. Lett. 2003; 82(17) 2847-2849.

[97] Eyidi D, Eibl O, Wenzel T, Nickel KG, Schlachter SI, and Goldacker W, Superconducting properties, microstructure and chemical composition of MgB_2 sheathed materials, Supercond. Sci. Technol. 2003; 16(7) 778-788.

[98] Pan AV, Zhou SH, Liu HK, and Don SX, Properties of superconducting MgB_2 wires: versus reaction technique, Supercond. Sci. Technol. 2003; 16(5) 639-644.

[99] Serquis A, Civale L, Hammon DL, Coulter JY, Liao XZ, Zhu YT, Peterson DE, and Mueller FM, Microstructure and high critical current of powder-in-tube MgB_2, Appl. Phys. Lett. 2003; 82(11) 1754-1756.

[100] Serquis A, Civale L, Hammon DL, Liao XZ, Coulter JY, Zhu YT, Peterson DE, and Mueller FM, Role of excess Mg and heat treatments on microstructure and critical current of MgB_2 wires, J. Appl. Phys. 2003; 94(6) 4024-4031.

[101] Suo HL, Beneduce C, Dhalle M, Musolino N, Genoud JY, and Flukiger R, Large transport critical currents in dense Fe- and Ni-clad MgB_2 superconducting tapes, Appl. Phys. Lett. 2001; 79(19) 3116-3118.

[102] Grasso G, Malagoli A, Ferdeghini C, Roncallo S, Braccini V, Siri AS, and Cimberle MR, Large transport critical currents in unsintered MgB_2 superconducting tapes, Appl. Phys. Lett. 2001; 79(2) 230-232.

[103] Li WX, Zeng R, Lu L, and Dou SX, Effect of thermal strain on J_c and T_c in high density nano-SiC doped MgB_2, J. Appl. Phys. 2011; 109(7) 07E108.

[104] Li WX, Zeng R, Lu L, Li Y, and Dou SX, The combined influence of connectivity and disorder on J_c and T_c performances in Mg_xB_2+10 wt % SiC, J. Appl. Phys. 2009; 106(9) 093906.

[105] Li WX, Zeng R, Lu L, Zhang Y, Dou SX, Li Y, Chen RH, and Zhu MY, Improved superconducting properties of powder-in-tube processed $Mg_{1.15}B_2$/Fe wires with nano-size SiC addition, Physica C 2009; 469(15-20) 1519-1522.

[106] Zeng R, Dou SX, Lu L, Li WX, Kim JH, Munroe P, Zheng RK, and Ringer SP, Thermal-strain-induced enhancement of electromagnetic properties of SiC-MgB_2 composites, Appl. Phys. Lett. 2009; 94(4) 042510.

[107] Pogrebnyakov AV, Redwing JM, Raghavan S, Vaithyanathan V, Schlom DG, Xu SY, Li Q, Tenne DA, Soukiassian A, Xi XX, Johannes MD, Kasinathan D, Pickett WE, Wu JS, and Spence JCH, Enhancement of the superconducting transition temperature of MgB_2 by a strain-induced bond-stretching mode softening, Phys. Rev. Lett. 2004; 93(14) 147006.

[108] Neumeier JJ, Tomita T, Debessai M, Schilling JS, Barnes PW, Hinks DG, and Jorgensen JD, Negative thermal expansion of MgB_2 in the superconducting state and anomalous behavior of the bulk Gruneisen function, Phys. Rev. B 2005; 72(22) 220505.

[109] Li Z and Bradt RC, Thermal expansion of the hexagonal (4H) polytype of SiC, J. Appl. Phys. 1986; 60(2) 612-614.

[110] Buzea C and Yamashita T, Review of the superconducting properties of MgB_2, Supercond. Sci. Technol. 2001; 14(11) R115-R146.

[111] Jorgensen JD, Hinks DG, and Short S, Lattice properties of MgB_2 versus temperature and pressure, Phys. Rev. B 2001; 6322(22) 224522.

[112] Williamson GK and Hall WH, X-ray line broadening from filed aluminium and wolfram, Acta Metall. Mater. 1953; 1)22-31.

[113] Blatter G, Feigelman MV, Geshkenbein VB, Larkin AI, and Vinokur VM, Vortices in high-temperature superconductors, Rev. Mod. Phys. 1994; 66(4) 1125-1388.

[114] Li WX, Li Y, Chen RH, Zeng R, Zhu MY, Jin HM, and Dou SX, Electron-phonon coupling properties in MgB_2 observed by Raman scattering, J. Phys.-Condens. Matter 2008; 20(25) 255235.

[115] Li WX, Li Y, Chen RH, Zeng R, Dou SX, Zhu MY, and Jin HM, Raman study of element doping effects on the superconductivity of MgB_2, Phys. Rev. B 2008; 77(9) 094517.

[116] Li WX, Zeng R, Poh CK, Li Y, and Dou SX, Magnetic scattering effects in two-band superconductor: the ferromagnetic dopants in MgB_2, J. Phys.-Condens. Matter 2010; 22(13) 135701.

[117] Shi L, Zhang HR, Chen L, and Feng Y, The Raman spectrum and lattice parameters of MgB_2 as a function of temperature, J. Phys.-Condens. Matter 2004; 16(36) 6541-6550.

[118] Allen PB, Neutron spectroscopy of superconductors, Phys. Rev. B 1972; 6(7) 2577-2579.

[119] Kortus J, Dolgov OV, Kremer RK, and Golubov AA, Band filling and interband scattering effects in MgB_2: Carbon versus aluminum doping, Phys. Rev. Lett. 2005; 94(2) 027002.

[120] McMillan WL, Transition temperature of strong-coupled superconductors, Phys. Rev. 1968; 167(2) 331-334.

[121] Allen PB and Dynes RC, Transition-temperature of strong-coupled superconductors reanalyzed, Phys. Rev. B 1975; 12(3) 905-922.

[122] Kortus J, Mazin II, Belashchenko KD, Antropov VP, and Boyer LL, Superconductivity of metallic boron in MgB_2, Phys. Rev. Lett. 2001; 86(20) 4656-4659.

[123] Osborn R, Goremychkin EA, Kolesnikov AI, and Hinks DG, Phonon density of states in MgB_2, Phys. Rev. Lett. 2001; 87(1) 017005.

[124] Brinkman A, Golubov AA, Rogalla H, Dolgov OV, Kortus J, Kong Y, Jepsen O, and Andersen OK, Multiband model for tunneling in MgB_2 junctions, Phys. Rev. B 2002; 65(18) 180517.

[125] Collings EW, Sumption MD, Bhatia M, Susner MA, and Bohnenstiehl SD, Prospects for improving the intrinsic and extrinsic properties of magnesium diboride superconducting strands, Supercond. Sci. Technol. 2008; 21(10) 103001.

[126] Li WX, Li Y, Chen RH, Yeoh WK, and Dou SX, Effect of magnetic field processing on the microstructure of carbon nanotubes doped MgB_2, Physica C 2007; 4601)570-571.

[127] Yeoh WK, Horvat J, Dou SX, and Munroe P, Effect of carbon nanotube size on superconductivity properties of MgB_2, IEEE Trans. Appl. Supercond. 2005; 15(2) 3284-3287.

[128] Li WX, Li Y, Zhu MY, Chen RH, Xu X, Yeoh WK, Kim JH, and Dou SX, Benzoic acid doping to enhance electromagnetic properties of MgB_2 superconductors, IEEE Trans. Appl. Supercond. 2007; 17(2) 2778-2781.

[129] Zhuang CG, Meng S, Zhang CY, Feng QR, Gan ZZ, Yang H, Jia Y, Wen HH, and Xi XX, Ultrahigh current-carrying capability in clean MgB_2 films, J. Appl. Phys. 2008; 104(1) 013924.

[130] Zeng XH, Pogrebnyakov AV, Zhu MH, Jones JE, Xi XX, Xu SY, Wertz E, Li Q, Redwing JM, Lettieri J, Vaithyanathan V, Schlom DG, Liu ZK, Trithaveesak O, and Schubert J, Superconducting MgB_2 thin films on silicon carbide substrates by hybrid physical-chemical vapor deposition, Appl. Phys. Lett. 2003; 82(13) 2097-2099.

[131] Flukiger R, Hossain MSA, and Senatore C, Strong enhancement of J_c and B_{irr} in binary MgB_2 wires after cold high pressure densification, Supercond. Sci. Technol. 2009; 22(8) 085002.

[132] Hossain MSA, Senatore C, Flukiger R, Rindfleisch MA, Tomsic MJ, Kim JH, and Dou SX, The enhanced J_c and B_{irr} of MgB_2 wires and tapes alloyed with $C_4H_6O_5$ (malic acid) after cold high pressure densification, Supercond. Sci. Technol. 2009; 22(9) 095004.

[133] Kovac P, Reissner M, Melisek T, Husek I, and Mohammad S, Current densities of MgB_2 wires by combined ex process, J. Appl. Phys. 2009; 106(1) 013910.

[134] Li WX, Zeng R, Zhang Y, Xu X, Li Y, and Dou SX, Evolution of electromagnetic properties and microstructure with sintering temperature for MgB_2/Fe wires made by combined *In-Situ*/*Ex-Situ* process, IEEE Trans. Appl. Supercond. 2011; 21(3) 2635-2638.

[135] Xu X, Kim JH, Dou SX, Choi S, Lee JH, Park HW, Rindfleish M, and Tomsic M, A correlation between transport current density and grain connectivity in MgB_2/Fe wire made from ball-milled boron, J. Appl. Phys. 2009; 105(10) 103913.

[136] Romano G, Vignolo M, Braccini V, Malagoli A, Bernini C, Tropeano M, Fanciulli C, Putti M, and Ferdeghini C, High-energy ball milling and synthesis temperature study to improve superconducting properties of MgB_2 *ex-situ* tapes and wires, IEEE Trans. Appl. Supercond. 2009; 19(3) 2706-2709.

[137] Li WX, Chen RH, Li Y, Zhu MY, Jin HM, Zeng R, Dou SX, and Lu B, Raman study on the effects of sintering temperature on the $J_c(H)$ performance of MgB_2 superconductor, J. Appl. Phys. 2008; 103(1) 013511.

[138] Chen RH, Zhu MY, Li Y, Li WX, Jin HM, and Dou SX, Effect of pulsed magnetic field on critical current in carbon-nanotube-doped MgB_2 wires, Acta Physica Sinica 2006; 55(9) 4878-4882.

[139] Zhang XP, Ma YW, Gao ZS, Yu ZG, Watanabe K, and Wen HH, Effect of nanoscale C and SiC doping on the superconducting properties of MgB_2 tapes, Acta Physica Sinica 2006; 55(9) 4873-4877.

[140] Li WX, Zeng R, Wang JL, Li Y, and Dou SX, Dependence of magnetoelectric properties on sintering temperature for nano-SiC-doped MgB_2/Fe wires made by combined *in situ*/*ex situ* process, J. Appl. Phys. 2012; 111(7) E7135-E7135.

[141] Dou SX, Pan AV, Zhou S, Ionescu M, Wang XL, Horvat J, Liu HK, and Munroe PR, Superconductivity, critical current density, and flux pinning in $MgB_{2-x}(SiC)_{x/2}$ superconductor after SiC nanoparticle doping, J. Appl. Phys. 2003; 94(3) 1850-1856.

[142] Dou SX, Pan AV, Zhou S, Ionescu M, Liu HK, and Munroe PR, Substitution-induced pinning in MgB_2 superconductor doped with SiC nano-particles, Supercond. Sci. Technol. 2002; 15(11) 1587-1591.

[143] Zhang Y, Dou SX, Lu C, Zhou H, and Li WX, Effect of Mg/B ratio on the superconductivity of MgB_2 bulk with SiC addition, Phys. Rev. B 2010; 81(9) 094501.

[144] Angst M, Bud'ko SL, Wilke RHT, and Canfield PC, Difference between Al and C doping in anisotropic upper critical field development in MgB_2, Phys. Rev. B 2005; 71(14) 144512.